The interaction of a large-scale nuclear wind with the high-velocity H II region G0.17+0.15

F. Yusef-Zadeh [1]★ Jun-Hui Zhao,[2] R. Arendt [3] M. Wardle,[4] M. Royster,[5] L. Rudnick [6] and J. Michail [1]

[1]*Department of Physics and Astronomy, Northwestern University, Evanston, IL 60208, USA*
[2]*Center for Astrophysics | Harvard-Smithsonian, 60 Garden Street, Cambridge, MA 02138, USA*
[3]*UMBC/GSFC/CRESST 2, Code 665, NASA/GSFC, 8800 Greenbelt Rd, Greenbelt, MD 20771, USA*
[4]*School of Mathematical and Physical Sciences, Centre for Astronomy and Space Technology, Macquarie University, Sydney NSW 2109, Australia*
[5]*Department of Physics, Sequaya Community College, Visalia, CA 93277, USA*
[6]*Minnesota Institute for Astrophysics, University of Minnesota, 116 Church St SE, Minneapolis, MN 55455, USA*

ABSTRACT

We investigate the nature of a Galactic Centre source, G0.17+0.15, lying along the northern extension of the radio arc near $l \sim 0.2°$. G0.17+0.15 is an H II region located towards the eastern edge of the radio bubble, embedded within the highly polarized Galactic Centre eastern lobe where a number of radio filaments appear to cross through the H II region. We report the detection of hydrogen and helium recombination lines with a radial velocity exceeding 140 km s^{-1} based on Green Bank Telescope and Very Large Array observations. The morphology of G0.17+0.15, aided by kinematics, and spectral index characteristics, suggests the presence of an external pressure dragging and shredding the ionized gas. We argue that this ionized cloud is interacting with a bundle of radio filaments and is entrained by the ram pressure of the radio bubble, which itself is thought to be produced by cosmic ray driven outflows at the Galactic Centre. In this interpretation, the gas streamers on the western side of G0.17+0.15 are stripped, accelerated from 0 to $\delta v \sim 35$ km s^{-1} over a time-scale roughly 8×10^4 yr, implying that ablating ram pressure is ~ 700 eV cm^{-3}, comparable to the $\sim 10^3$ eV cm^{-3} cosmic ray driven wind pressure in the Galactic Centre region.

Key words: magnetic fields – radiation mechanisms: non-thermal – cosmic rays – Galaxy: centre – radio lines: ISM.

1 INTRODUCTION

Energetic processes have produced the large-scale Fermi γ-ray bubbles towards the nucleus of the Galaxy (Su, Slatyer & Finkbeiner 2010). The origin of this kpc-scale structure is thought to be a nuclear wind driven by either nuclear activity or star formation (Crocker & Aharonian 2011; Yang, Ruszkowski & Zweibel 2013). Nuclear winds are well recognized in many star-forming galaxies (Veilleux, Cecil & Bland-Hawthorn 2005), and the evidence for this hypothesis comes from high-velocity clouds exceeding $|v_r| \sim 300$ km s^{-1} at high latitudes entrained in the Fermi bubble (McClure-Griffiths et al. 2013; Di Teodoro et al. 2020). Lower velocity $\sim$150 km s^{-1} H I clouds entrained in the Fermi bubble have also been detected closer to the Galactic Centre suggesting increasingly higher velocities at higher latitudes (Di Teodoro et al. 2020; Lockman, Di Teodoro & McClure-Griffiths 2020).

Bipolar X-ray emission filling a 400-pc radio bubble emerging from the Galactic Centre has been detected (Heywood et al. 2019; Ponti et al. 2019). The question is whether a large-scale nuclear wind is also responsible for its origin. In this case, high cosmic ray pressure is thought to be driving a large-scale wind (Heywood et al. 2019; Yusef-Zadeh & Wardle 2019). The cosmic ray pressure

in the Galactic Centre region is much higher than the gas pressure (Oka et al. 2005; Yusef-Zadeh & Wardle 2019), leading to a scenario in which the gas is dragged along by escaping cosmic rays and forms a nuclear wind (Kulsrud & Cesarsky 1971; Everett, Schiller & Zweibel 2010; Zweibel 2017). Unlike the Fermi bubble, however, there is no evidence of high-velocity entrained clouds associated with the nuclear wind producing the X-ray-filled radio bubble. Radio recombination line (RRL) observations of warm ionized gas in the eastern and western, high Galactic latitudes, lobes, identified at the edges of the radio bubble (Sofue & Handa 1984; Tsuboi et al. 1986), show low velocities ranging between $\sim$20 and -20 km s^{-1}, respectively (Alves et al. 2015). These low velocities are inconsistent with the expectation that the Lobes are byproducts of the nuclear wind, suggesting that the Lobes may not lie in the Galactic Centre (Tsuboi et al. 2020).

Although the radio bubble could result of a Galactic Centre nuclear wind, it is important to identify high-velocity clouds that are interacting with the underlying wind that expands the bubble. We have identified an H II region, G0.17+0.15, showing a radial velocity of $\sim$130 km s^{-1} suggesting that G0.17+0.15 lies in the Galactic Centre. This source lies $\sim 4'$ (~ 10 pc) towards high Galactic latitudes (north) of the prominent thermal, ionized Arches at -20 km s^{-1} (Pauls & Mezger 1980; Yusef-Zadeh, Morris & van Gorkom 1987; Lang, Goss & Morris 2001) and appears to be located within large-scale, high-velocity ^{12}CO molecular clouds

traced in molecular line surveys of the Galactic Centre (Bally et al. 1988; Sofue 1995; Oka et al. 1998; Henshaw et al. 2016; Sormani et al. 2019; Veena et al. 2023).

The high-velocity, spectral index and polarization characteristics suggest that G0.17+0.15 is a Galactic Centre object interacting with non-thermal radio filaments (NRFs). We report a strong helium radio recombination line emission from G0.17+0.15, likely be one of the strongest helium recombination line emission in the Galactic Centre region. The morphology and kinematics of G0.17+0.15 show evidence of an external flow dragging and shredding the ionized gas at the edges of the H II region. We argue that the ram pressure of the cosmic ray driven wind inflating the radio bubble is able to explain the velocity difference across the H II region and is sufficient to accelerate the H II cloud.

In this paper, we explore one possibility that can explain the results of our measurements. While each of the observational findings can be explained in alternate ways, such as infall motion of the cloud and/or H II region from its high-latitude location towards the Galactic Centre, the nuclear wind H II interpretation is interesting enough that we focus here in exploring its plausibility as opposed to arguing that it is a unique interpretation. In particular, we focus on G0.17+0.15 and present results of RRL measurements towards G0.17+0.15. This cloud is localized towards the eastern lobe, near $l \sim 0.2°$. We argue here that the G0.17+0.15 cloud is embedded within the eastern lobe, which is dominated by a mixture of thermal and non-thermal radio emission, and that the filaments of the radio arc [$l \sim 0.2°$ (galactic longitude)] are interacting with a thermal H II region, G0.17+0.15. We have also studied infrared (IR) counterparts to the ionized gas and the energetics needed to produce gas and dust emission. A true physical interaction will tell us about the nature of cosmic ray driven outflows at the Galactic Centre and the possible resemblance of the radio and Fermi γ-ray bubbles.

2 OBSERVATIONS AND DATA REDUCTIONS

We used the Green Bank Telescope (GBT), MeerKAT, and the Very Large Array (VLA) to study the continuum emission, radio recombination line emission, and spectral index properties, as described below.

2.1 Continuum

We have used 1.28 GHz radio continuum images of the Galactic Centre with 4 and 6 arcsec resolution based on unfiltered and filtered data taken with MeerKAT, respectively (Heywood et al. 2022; Yusef-Zadeh et al. 2022). Details of filtered and unfiltered images are described in Heywood et al. (2022) and Yusef-Zadeh et al. (2022). We also used the VLA wideband data observed at 6 GHz (*C* band) and 10 GHz (*X* band).

2.1.1 6 GHz-band VLA data

The *C*-band observations with the VLA were carried out at three epochs: 2022-06-28, 2022-07-03, and 2022-07-04 in the A-array configurations with a total on-source time of 150 min, sampling the spectral polarization data of RR, RL, LR, and LL with 64 channels of 2-MHz width in each of 32 sub-bands. The total bandwidth of the continuum data is 4 GHz centred at 6 GHz. The VLA data reduction was conducted using CASA (The CASA Team 2022). The high-resolution *C*-band data were initially calibrated using the VLA pipeline program for the gains, bandpass, polarization leakages, and phase offsets as well as flux-density and absolute linear polarization angle (the results of these measurements will be given in a future

paper discussing compact radio sources in the Galactic Centre). The residual errors were further corrected using better models, including an extended structure in addition to a point-like core of the calibrators J1733−1304 and J1744−3116 following the procedure described by Zhao, Morris & Goss (2019). Then, the H II complex and its surroundings were imaged and cleaned using *tClean*, a CASA program, weighting the visibilities with a robustness parameter $R = 0.65$ (Briggs 1995a, b). The rms noise of the final image is 3.5 μJy beam^{-1} convolved to a full width at half-maximum (FWHM) beam of 1 arcsec × 0.5 arcsec with position angle (PA) of 0°. Polarization and in-band spectral index measurements will be given elsewhere. The phase centre is at RA (J2000) = 17:45:26.400; Dec. (J2000) = −28:42:46.500.

2.1.2 10 GHz-band VLA data

The *X*-band observations were carried out in the D and C array configurations at seven epochs: 2022-07-26, 2022-07-29, 2022-07-30, 2022-09-30, 2022-10-01, 2022-10-09, and 2022-10-16. The telescope system was set-up for simultaneously observing the hydrogen recombination lines at the 11 Hα ($83 < n < 92$) lines in each of 11 sub-bands in the frequency range between 8 and 12 GHz. Each sub-band consists of 1280 channels with a width of 0.05 MHz (a mean velocity width of $\sim$1.5 km s^{-1}). An effective bandwidth for the continuum data is therefore $\sim$0.70 GHz. Corrected for residual errors, the *X*-band visibilities were used to construct an image for the continuum emission, achieving an rms noise of $\sim$10 μJy beam^{-1}, convolved to an FWHM beam of 4.6 arcsec × 2.1 arcsec (PA $\sim$ 10°). The phase centre is at RA (J2000) = 17:45:26.40; Dec. (J2000) = −28:42:46.50.

2.2 Radio recombination line (RRL) data

2.2.1 10 GHz-band GBT data

RRL observations of G0.17+0.15 using the GBT at 10 GHz were part of an (unpublished) targeted survey of Galactic Centre sources with the GBT in 2005. The observations detected six Hα ($87 \leq n \leq 92$) and nine Hβ ($109 \leq n \leq 117$) transitions found within the *X*-band receiver's bandpass (8.0–10.0 GHz) over multiple IFs. An On-Off observing technique with a roughly $\sim$70 arcsec beam was employed for calibration and the recombination lines were co-added in GBTIDL to improve sensitivity. The total achieved velocity range exceeded 1000 km s^{-1} with a velocity resolution of less than 1 km s^{-1} after hanning smoothing. A sparsely sampled map was produced with 32 pointings towards G0.17+0.15 with a final spatial resolution of roughly 1.6 arcmin (FWHM).

2.2.2 10 GHz-band VLA data

We followed GBT observations with high-resolution RRL observations of 11 hydrogen recombination lines Hα ($82 \leq n \leq 92$) over a 4-GHz bandwidth of *X* band with the VLA, as described in Section 2.1.2. The corrections for the residual errors were done on the basis of sub-bands using the gains and bandpass derived in corrections for the continuum visibility data. The corrected *uv*-data observed at the seven epochs were combined.

The line free channels were chosen to make linear fitting to the continuum baselines, in the uv-domain across the 1280 spectral channels for each of the 11 sub-bands. This was followed by removing the continuum emission using the linear-fitting results. The fitting and continuum subtraction were carried out by utilizing the CASA task UVCONTSUB. Then, the 11 spectral line cubes were

transformed to the local standard of rest (LSR) velocity frame in the uv-data domain while setting up the rest frequency using the corresponding H α-transitions. The spectral line visibilities were regridded in the velocity coordinate with velocity width of 2 km s^{-1}. The eleven H α-line image cubes were constructed using *tClean* in a velocity range from -200 to 400 km s^{-1}, and the dirty image cubes were cleaned using the Hogbom algorithm (Högbom 1974), achieving in constructing and cleaning a typical rms noise in the range between 0.25 and 0.5 mJy beam^{-1} depending on the noises of sub-band data. We also used a linear function to interpolate the robustness weight parameter R across the 11 sub-bands so that the baseline visibilities of 11 transitions are properly weighted to produce a synthesized beam equivalent to that of $R = 2$ for the H α line image. In Appendix A, we describe how the RRL image cubes of 11 RRLs were stacked in order to enhance the signal-to-noise ratio.

2.3 In-band spectral index

Details of MeerKAT observations, data reductions, and images (unfiltered) are presented in Heywood et al. (2022). Using a filtering technique, filtered MeerKAT images are presented in Yusef-Zadeh et al. (2022). In-band spectral indices are determined from broad bandwidth 20 cm data using unfiltered and filtered MeerKAT data with a resolution of 6.4 and 8 arcsec, respectively (Heywood et al. 2022; Yusef-Zadeh et al. 2022).

2.3.1 VLA data

Details of in-band spectral index using VLA wideband data can be found in Appendix A. We present below spectral indices of unfiltered and filtered images.

3 RESULTS

Here, we mainly focus on the physical relationship between NRFs bundled together by the Galactic Centre lobe (GCL) and the H II region G0.17+0.15, located in the eastern side of the high-Galactic latitudes GCL.

3.1 G0.17+0.15

Multiple morphological arguments given below favour an interaction between G0.17+0.15, resembling a ring with clumpy structure, and the NRFs of the radio arc. However, morphological arguments alone tend to be inconclusive, thus, we will show structural details of G0.17+0.15 aided by kinematics, spectral index, and rotation measure (RM) measurements to argue that G0.17+0.15 is a candidate interaction site. This remarkable high velocity ionized cloud G0.17+0.15 shows similar characteristics to high-velocity clouds associated with the γ-ray bubbles.

3.1.1 Morphology

Fig. 1(a) shows a degree-scale panoramic view of the radio bubble tracing the edge of the northern GCL and the radio bubble at 1.28 GHz (Heywood et al. 2019). In this MeerKAT image, we note G0.17+0.15 and non-thermal filaments as well as the thermal Arches to the south. This H II region, G0.17+0.15 with its ring-like appearance, lies along the eastern GCL, and appears to be embedded within a large number of vertical non-thermal filaments.

Figs 1(b) and (c) show unfiltered and filtered close-up views of the H II region over a ~6 arcmin $\times$ 6.6 arcmin field at 1.28 GHz. The H II region resembles a clumpy, ring-like envelope with a bowshock exterior to the ring (see also fig. 3 of Yusef-Zadeh & Morris 1988). We note a gently bent bundle of filaments with their wavy structure along the western edge of G0.17+0.15 extending to high latitudes $b > 0.28°$. There are also other isolated non-thermal filaments noted to the west of the ring that do not appear to be related to G0.17+0.15. These filaments to the west of the ring at constant latitudes are G0.147 + 0.15, and G0.139 + 0.15 roughly 1.4 and 2 arcmin from the ring, respectively, gently bend but are not distorted and do not have a wavy appearance (see Figs 1b and c). Fig. 2(a) shows a colour image with major features are labelled and Fig. 2(b) shows a schematic diagram showing structural details discussed here.

Using the VLA, another rendition, a G0.17+0.15 with a resolution of 4.6 arcsec $\times$ 2.1 arcsec at 10 GHz is shown in Fig. 3(a). A close-up view of this image in Fig. 3(b) shows clumpy distribution of the ring, with a southern and northern shell-like structures and two linear features with an extent of ~0.6 arcmin running vertically near $l = 0.162°$. The brightest continuum emission is at G0.170 + 0.149 which lies at the southern shell of the ring. The disjoint linear features give the appearance that they are connected to the arc-like structure at the SW of the ring (see Figs 2a and 3b). We also note two dark circular spots with a diameter of ~12 arcsec each centred at G0.166 + 0.168, G0.152 + 0.149, respectively, in the western half of the ring. These dark spots may trace dense molecular gas or a cavity in the ionized gas (Yusef-Zadeh 2012). The southern-half of the ring is sharper in the south than in the north, giving the appearance of a bow-shock structure.

Based on the 1.28 and 10 GHz continuum images, we make morphological arguments that there is interaction between the filaments and G0.17+0.15. First, the wavy pattern or meandering of the filaments at the western edge of the ring (see Fig. 1c) could be due to an interaction. In this picture, the distortion of the filaments results from the encounter of the filaments with G0.17+0.15. Second, the western edge of the ring is brighter than the eastern side by a factor of 3–4. The two linear features near G0.162 + 0.159 and G0.159 + 0.152 with an extent of 0.6 arcmin are disjoint from the ring. The linear features could be produced by the ionized gas at the western edge of the ring being stripped and dragged along the direction of the bundle of NRFs. In Section 3.1.3, the kinematics of these linear features are described. Third, we note that the eastern half of the ring shows five short, parallel finger-like features running perpendicular to the ring with typical lengths of ~18 arcsec (see Figs 1b and c) and surface brightness ~0.5–0.8 mJy beam^{-1} at 1.28 GHz. These finger-like features near G0.176 + 0.158 are oriented along the vertical filaments of the Radio Arc suggesting that ring material is stripped off by an external pressure and dragged along the magnetic field lines of NRFs. The finger-like and two linear features are suggestive of ablated features (see Fig. 2b). Fourth, several NRFs appear to arise from thermal Arches near G0.176 + 0.091 and disappear at the southern edge of the ring at three locations (G0.167 + 0.147, G0.172 + 0.148, and G0.177 + 0.091), giving the appearance that they are supporting the ring from the south (see supporting filaments in Fig. 2). Multiple filaments with diffuse emission at the westernmost edge of the ring G0.154 + 0.150 bend with a wave-like structure along their higher Galactic latitude extension. Meandering of the total and polarized intensities of NRFs have also been argued as a possible sign of an interaction (Yusef-Zadeh & Morris 1988). A gentle wave-like bending of NRFs at the western edge of the ring, a north–south bow-shock appearance of the ring, termination of the filaments at the southern edge of the ring and finger-like vertical structure on the eastern side of the ring all suggest the impact of an external source of pressure, directed from the south, impacting the H II region (see Fig. 2b).
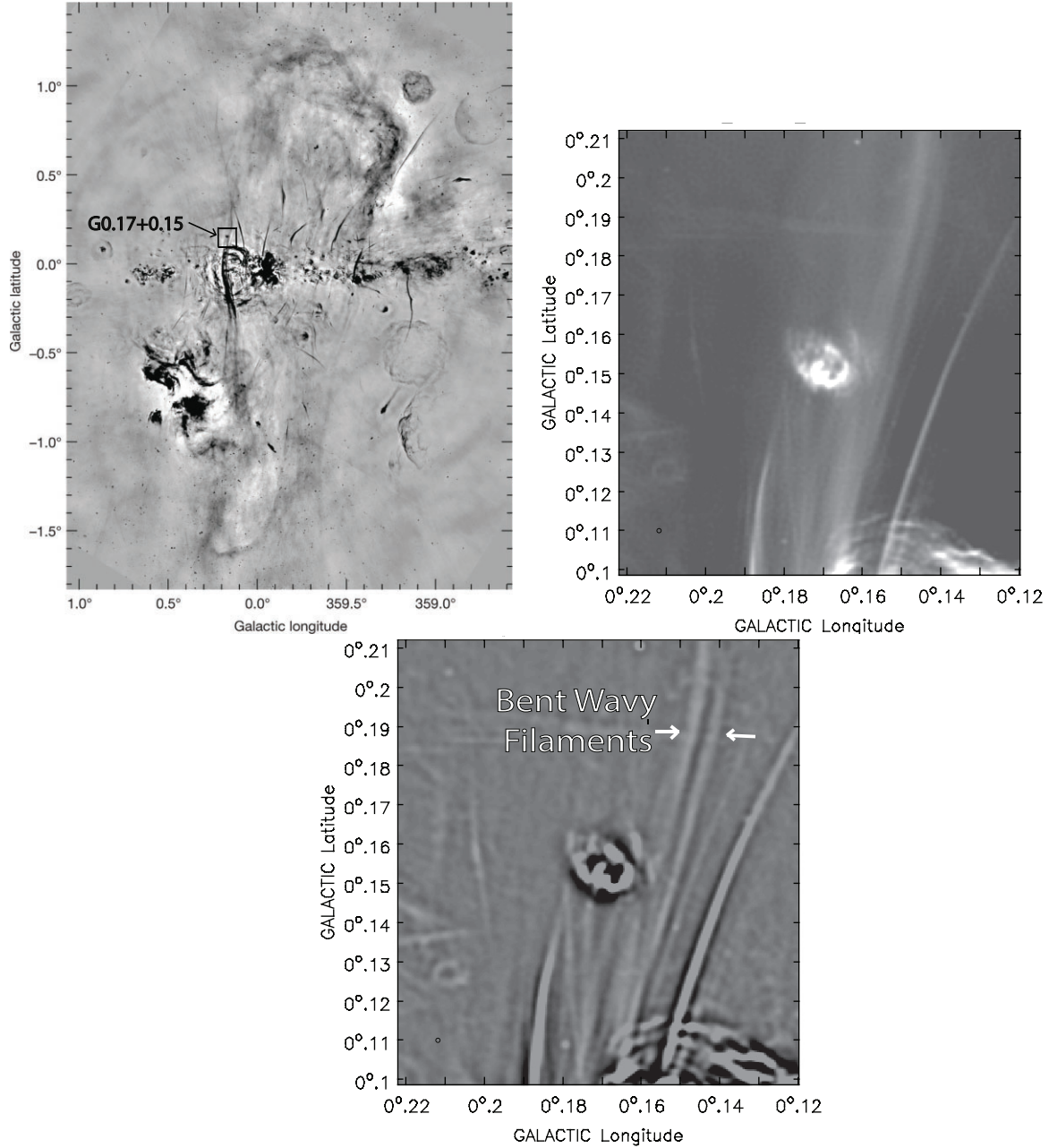
Figure 1. *(Top Left a)* A 1.28 GHz mosaic of the radio bubble with a resolution of 4 arcsec (fig. 1 of Heywood et al. 2019). G0.17+0.15 is shown along the northern extension of the Radio Arc near $l \sim 0.2°$. A rectangular box shows the region surrounding G0.17+0.15. (Heywood et al. 2019; Yusef-Zadeh et al. 2022). *(Top Right b)* A $0.1° \times 0.11°$ grey-scale view of G0.17+0.15 showing multiple filaments to the west of the H II region G0.17+0.15. *(Bottom c)* A filtered image of (b) showing three supporting filaments disappear at three positions on the ring (see also the diagram in Fig. 2b). Starting from the south, the bent wavy filaments appear to be deflected to the west of G0.17+0.15 and the return to a northward direction after passing the region. Two arrows point to these filaments. The small open circles in (b) and (c) show the size of the synthesized beam using CASA. The field of view shown as a box in (a) is displayed in (b) and (c).

We also note that the size of the ring is similar to the span of the bundle of filaments that are grouped together, suggesting that G0.17+0.15 is embedded within a large number of parallel filaments. An east–west asymmetry in the brightness distribution of NRFs crossing the H II region is similar to that of the ring itself, suggesting that the two are related. As such, the western edge of the ring and NRFs to the west of the ring show an imprint of an interaction.

To summarize, a number of morphological arguments suggest that the non-thermal filaments are physically interacting with G0.17+0.15:

(i) Three vertical filaments terminate at the location of the ring. This suggests that the filaments are interacting with the ring from the south and are prevented from continuing to the north.

(ii) The western half of G0.17+0.15 is brighter than the eastern half. Similarly, the large-scale bundle of filaments is also brighter on the western edge of the ring.

(iii) Isolated, short, vertical features north-west of the ring G0.17+0.15 suggest that they are dragged away from the ring by the bundle of filaments. Similarly, vertical fingers of ionized gas in the eastern half of the H II region suggest that they are likely stripped and dragged along the magnetic field direction of NRFs.
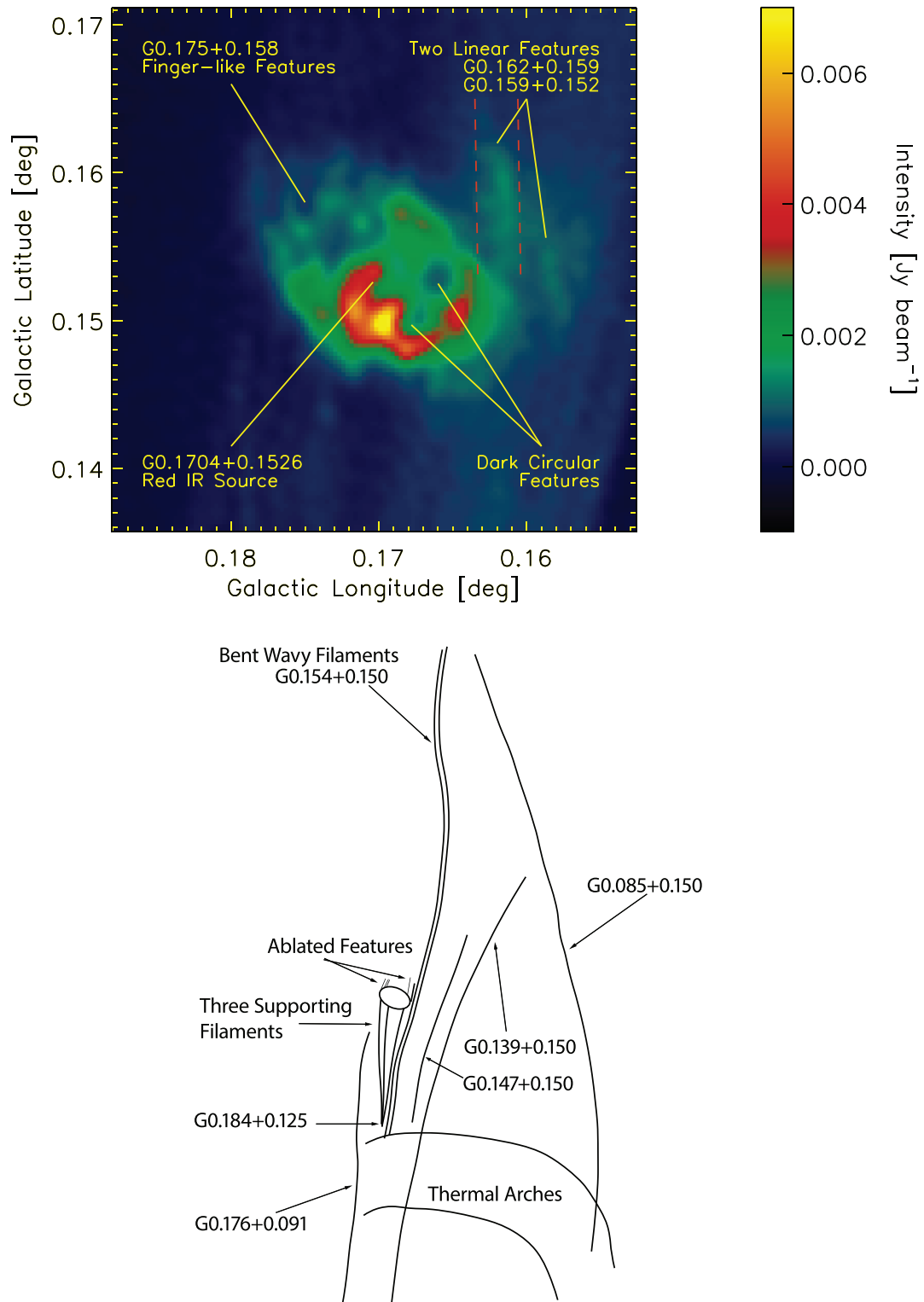
Figure 2. *(Top a)* A close-up continuum view of G0.17+0.15 at 1.28 GHz with a resolution of 0.4 arcsec showing its clumpy ring-like envelope and a bow-shock structure within the ring. Major features in the H II region are labelled. The colour bar units are in Jy beam^{-1}. The parallel lines (red dashed lines) indicate the region from which position-velocity image is constructed, as shown in Fig. 7. *(Bottom b)* A schematic diagram showing the features associated with G0.17+0.15 and its surrounding filaments.
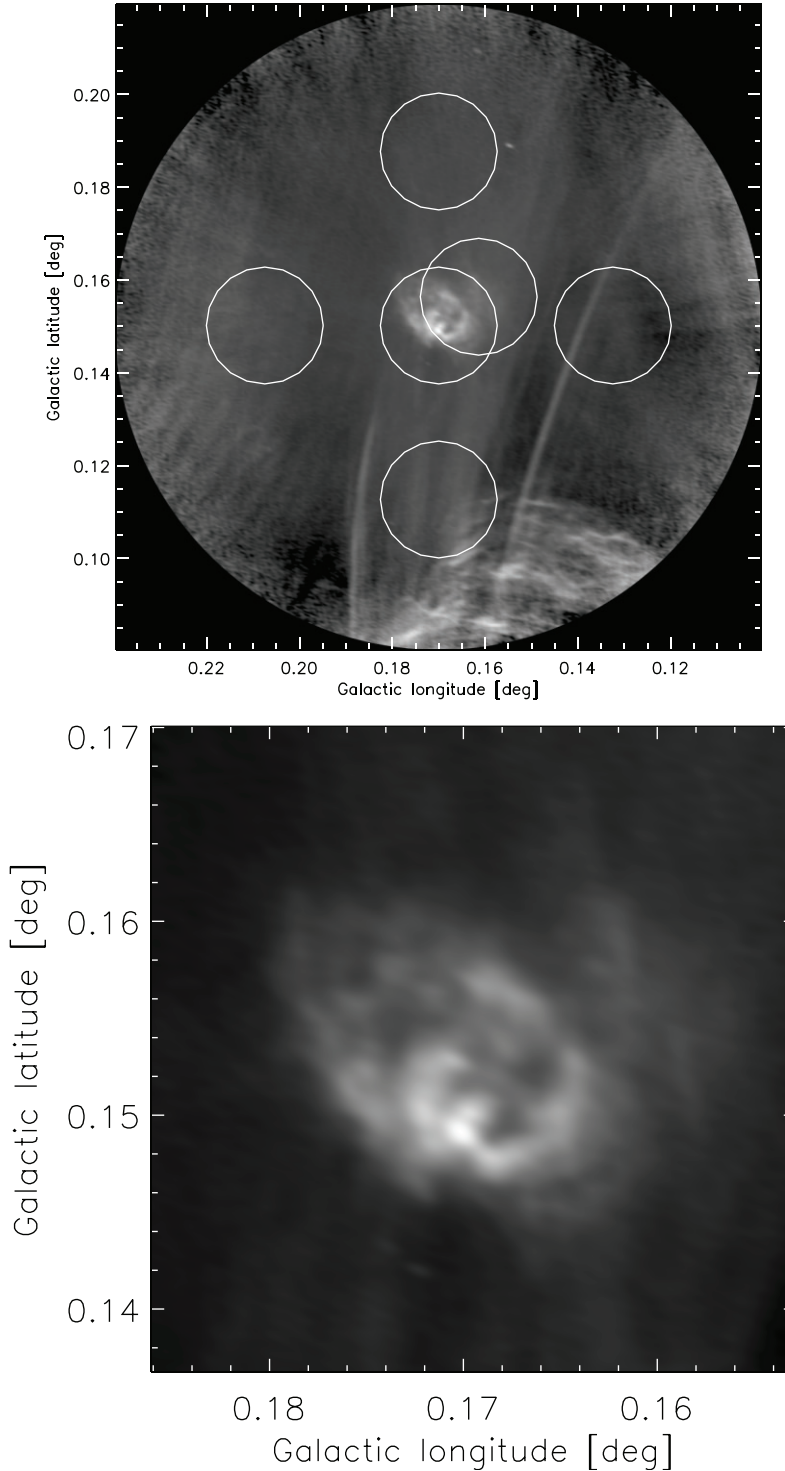
Figure 3. *(Top a)* VLA image of G0.17+0.15 at 10 GHz. The image is convolved with a beam of FWHM = 4.6 arcsec × 2.1 arcsec (PA = 68.6°). The phase centre is $l = 0.170°$, $b = 0.150°$ or RA (J2000) = 17:45:26.40; Dec. (J2000) = −28:42:46.5. The rms noise σ_{rms} is 10 μJy beam^{-1}. Circles drawn on the figure indicate the positions from which six spectra (see Fig. 4) were extracted. The size of a circle represents the GBT beam FWHM = 1.6 arcmin. *(Bottom b)* A close-up view of (a) showing clumpy structure as well as an arc-like halo structure that surrounds the southwestern edge of the ring.

(iv) The bundle of non-thermal filaments along the western edge of G0.17+0.15 are distorted displaying a wavy pattern with a wavelength of ∼10 arcmin (24 pc). This pattern is not detected along the filaments that do not intersect with G0.17+0.15.

Morphological arguments are always difficult to confirm. However, kinematic data provide additional support for the interaction picture. We first present low-spatial resolution recombination line data taken with the GBT, followed by higher resolution data taken with the VLA.

Table 1. Gaussian fits to integrated RRL spectrum per 1.6 arcmin beam.

| Name | Centre position | | | Gaussian fits | | Comments |
	l (deg)	b (deg)	$v \pm 1\sigma$ (km s^{-1})	Peak flux $\pm 1\sigma$ (mJy)	FWHM $\pm 1\sigma$ (km s^{-1})	
Centre	0.1700	0.1502	3.1 ± 0.03	4.2 ± 0.05	19.9 ± 0.16	Hα ($87 < n < 93$)
–	–	–	128 ± 0.37	16.4 ± 0.78	25.0 ± 2.05	Hα ($87 < n < 93$)
South	0.1700	0.1127	-12.8 ± 0.12	18.8 ± 0.11	40.1 ± 0.67	Hα ($87 < n < 93$)
North	0.1700	0.1877	7.5 ± 0.42	8.0 ± 0.23	12.6 ± 1.26	Hα ($87 < n < 93$)
East	0.2075	0.1502	127.0 ± 6.18	2.1 ± 0.075	38.0 ± 34.3	Hα ($87 < n < 93$)
West	0.1325	0.1502	x	x	x	Background noise
North-west	0.1614	0.1564	3.5 ± 0.41	4.5 ± 0.13	19.1 ± 0.3	Hα ($87 < n < 93$)
–	–	–	131.0 ± 0.04	14.1 ± 0.06	24.3 ± 0.24	Hα ($87 < n < 93$)

3.1.2 GBT kinematics: detection of high velocity ionized gas

Figs 4(a) and (b) show six spectra taken with the GBT towards G0.17+0.15, each separated by one 86.4 arcsec beam with the exception of the north-west spectrum being offset from the centre by a fraction of the beam width. The fitted spectra show a high-velocity ~ 128 km s^{-1} component, localized to the ionized ring, and a low-velocity components, ~ 3.1, 7, and -12 km s^{-1} components, which are discussed below. This relatively high velocity ionized gas was first reported by Royster et al. (2011). Columns 1–6 of Table 1 show the location of each spectrum, and the parameters of Gaussian fits: the centre velocity, peak flux density integrated over one beam, and the linewidth. The high intensity ratio of the low-velocity features with respect to high-velocity component (~ 30 per cent) in the centre and north-west positions suggests that the spectral features within the large GBT beam, near zero km s^{-1} are plausibly the helium recombination line mixed in with other lines from heavier species, such as C II. These lines are found in a larger, cooler and photodissociation regions surrounding the H II region as well as in the extended Galactic background and foreground RRLs throughout the Galactic Centre region (Royster et al., in preparation). If a slightly bigger region were selected, the 0 km s^{-1} diffuse gas would have been detected. The 0 km s^{-1} diffuse gas has also been detected in the $R(1, 1)$ line of H$_3^+$ absorption throughout the CMZ and has been argued to lie in the Galactic Centre region (Oka et al. 2005; Oka & Geballe 2020).

We note that the spectrum centred at G0.161 + 0.156 (north-west position on Fig. 4) shows two adjacent high-velocity components to the north-west position of G0.17+0.15. The highest velocity component disappears to the east of the H II region. We note an east–west asymmetry in the radial velocity of ionized gas in the ring. The highest velocity ~ 132 km s^{-1} component is detected to the north-west of the ring when compared to the eastern spectrum with a velocity of 127 km s^{-1}. A larger velocity difference is noted in high-resolution VLA data discussed in Section 3.1.3.

Another interesting asymmetry in the distribution of ionized gas outside the ring is noted in the six spectra displayed in Figs 4(a) and (b). The low velocity component near 0 km s^{-1} runs in the centre of the H II region and along the north–south direction outside G0.17+0.15. The linewidth of the south spectrum is broad because of contamination by the negative velocity ionized gas associated with the thermal Arches. The spectrum of the position centred on G0.17+0.15, located ~ 4 arcmin north of the negative velocity -20 km s^{-1} ionized gas cloud associated with the thermal Arches, is shown in Figs 4(a) and (b). The nature and location of the pervasive low-velocity component in the Galactic Centre is not established (Law et al. 2009; Alves et al. 2015; Oka et al. 2019), but the limited RRL available data suggest a possible association between the two components. In this picture, the low-velocity component is produced

by weak population inversion. The continuum flux for the central pointing is 0.5 Jy beam^{-1}, implying a line-to-continuum ratio of 0.8 per cent. The continuum flux for the east, west and south pointings are 0.06, 0.02, and 0.2 Jy beam^{-1}, suggesting peak RRL fluxes of 0.5, 0.2, and 1.6 mJy beam^{-1}, respectively. The predicted levels fall short of detection limits for the east and west pointings, while the predicted RRL component for the south pointing is swamped by the contribution from the thermal Arches.

The low-velocity component of the centre spectrum could be due to helium recombination line emission which occurs at frequencies that are shifted by -122 km s^{-1} relative to their hydrogen counterparts, This would be an unfortunate coincidence of a low-velocity pervasive component and helium line in G0.17+0.15. To test this, we used the VLA to localize the low-velocity component towards the H II region.

3.1.3 VLA kinematics: high velocity gas, and detection of helium recombination lines

Fig. 5(a) shows the Hα line intensity in the channel image at 126 km s^{-1} with the peak of the hydrogen RRL having S/N ratio ~ 50. A velocity profile at the peak emission is shown in Fig. 5(b) where we report a $> 5\sigma$ helium line detection. The reason that this line is unlikely to be due to hydrogen recombination line emission is that the emission is localized to the brightest region of the H II region. The zero km s^{-1} hydrogen RRL is extended and is seen throughout the Galactic Centre. Contours of the helium line emission (black) are superimposed on Fig. 5(a), suggesting that the integrated helium line intensity appears to be extended along the southern edge of G0.17+0.15, peaking at G0.17172 + 0.15105. This emission is localized only to the brightest region of G0.17+0.15, unlike the diffuse, pervasive zero km s^{-1} feature that is seen throughout the Galactic Centre (Law et al. 2009).

Two Gaussians were fitted to the line profile at the peak emission, giving integrated line flux values of 15 ± 3.0 and 200 ± 3 mJy km s^{-1} for the helium and hydrogen lines, respectively, with effective FWHM Gaussian widths of 25.3 ± 0.5 km s^{-1} for both lines. Thus, a value of ~ 7 per cent is inferred for the ratio of singly ionized helium line to the hydrogen line. This implies that this spectral feature is likely from the helium recombination line within the H II region.

Fig. 6 shows the results from the stacked RRL cube with an rms noise of 65 µJy beam^{-1}. The top panels show the 24 channel images at the LSR velocity from 106 to 152 km s^{-1} among the 300 channel images in the RRL cube in a velocity range between -200 and 400 km s^{-1}. The bottom right image shows the line emission integrated between 106 and 152 km s^{-1}. The brightest line intensity is localized to the south of the ring near G0.170 + 0.149. The line profiles are broader in the southern shell.
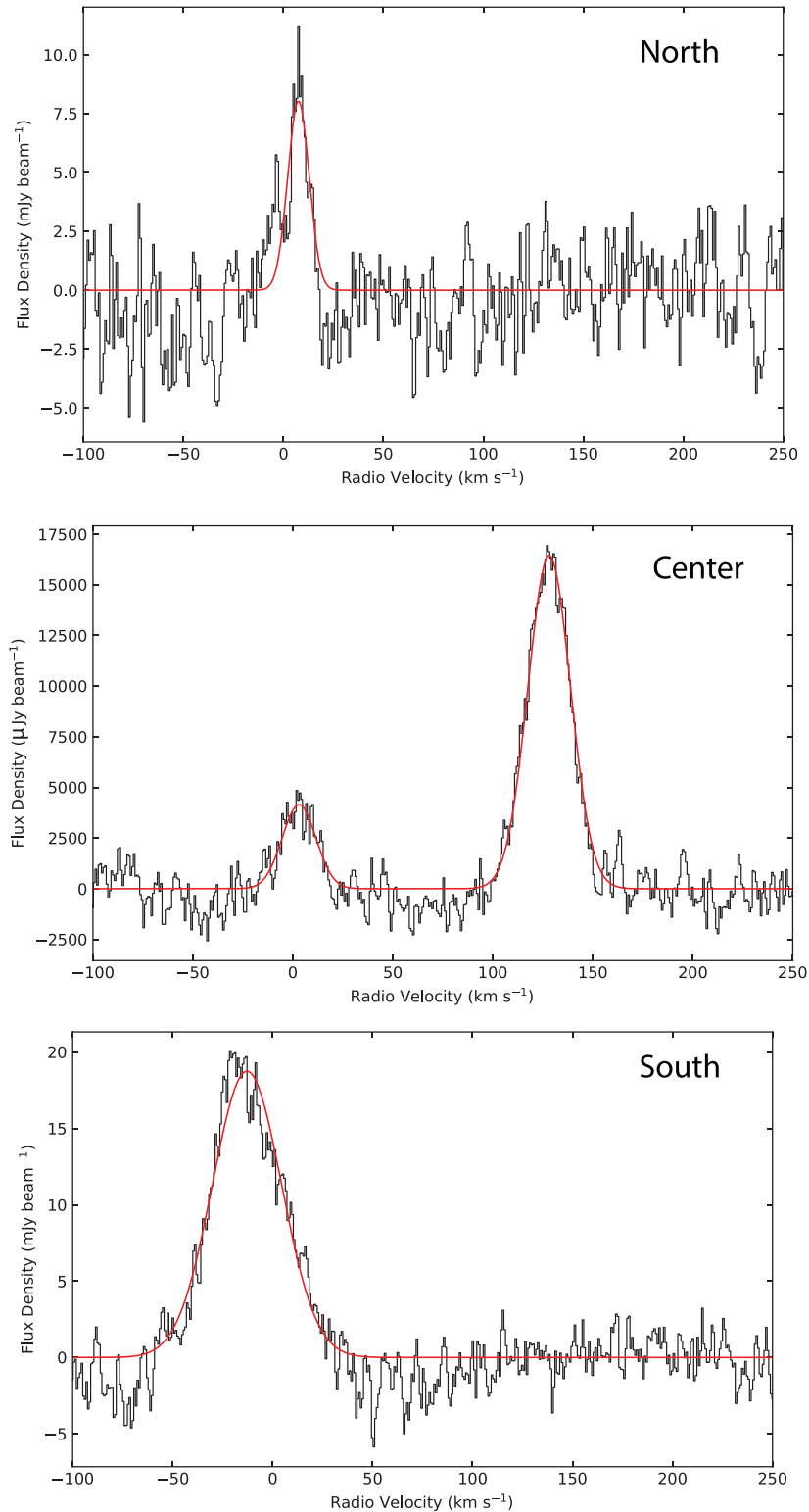
Figure 4. *(a)* Spectra of H α RRL emission per one 1.6 arcmin beam from three positions (centre, north, and south) covering the H II region. Red curves show Gaussian fits to each spectrum and fit parameters can be found in Table 1 (the units in the centre spectrum is in µJy beam^{-1} and all others in mJy beam^{-1}). The positions from Table 1 are marked as circles on Fig. 3(a). The size of the circle corresponds to the beam.

Fig. 7 shows the velocity profiles of three positions as indicated on the integrated line intensity image in the lower right corner of Fig. 6. The velocity profiles of the northern and southern shells of the ring give $v_{\rm LSR} \sim 126$ and ~ 129.5 km s^{-1}. The line emission is twice as strong in the south than in the northern shell of the ring. The Gaussian fitted linewidths of the southern and northern positions are 26 and 22 km s^{-1}, respectively. The Gaussian fit to the third position centred on the faint linear feature shows a peak velocity of ~ 146 km
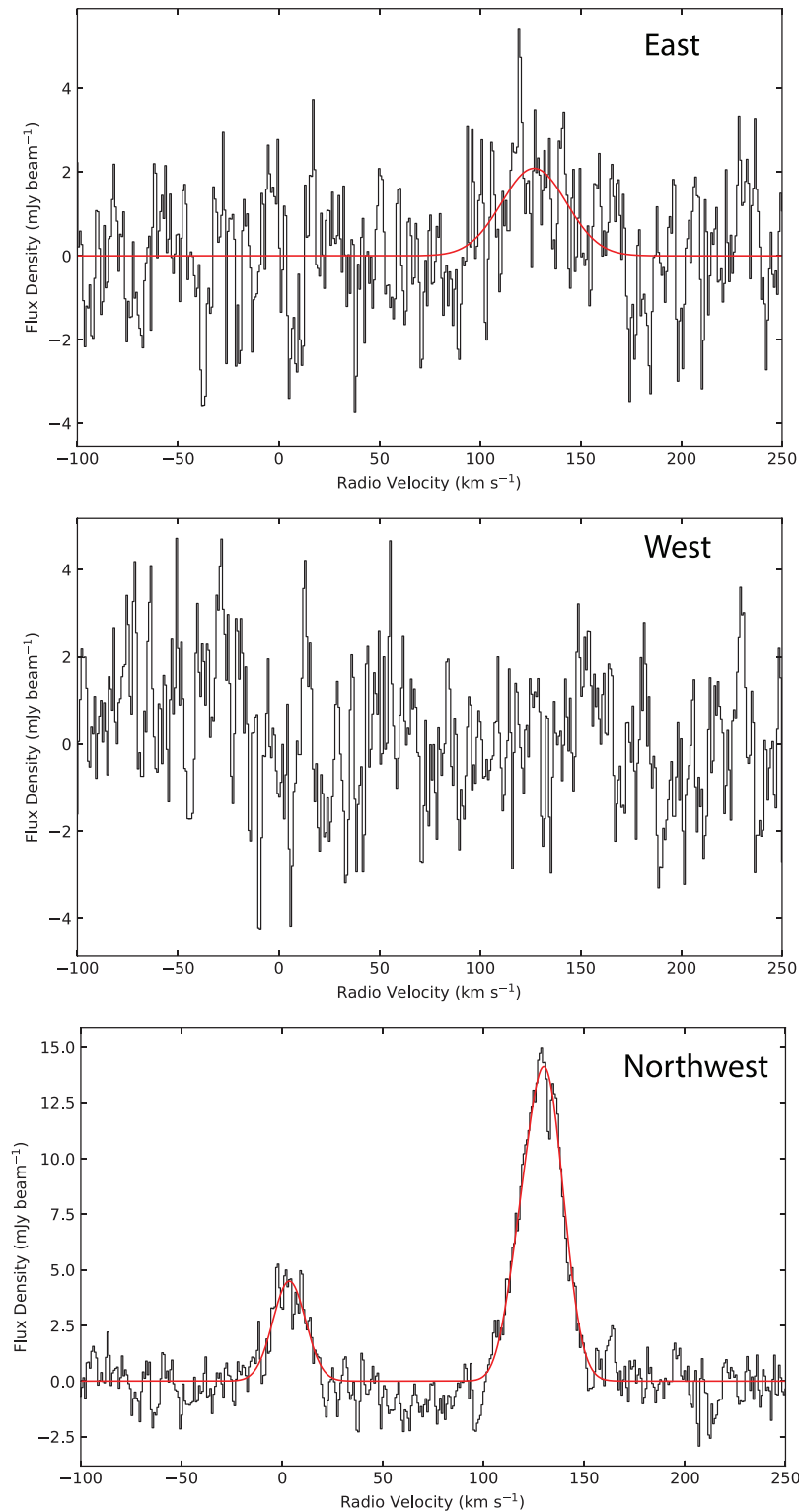
Figure 4. *(b)* Same as (a) except for three different positions (east, west, and north-west).

s^{-1}. This is the highest velocity of ionized gas detected towards the H II region. The position velocity diagram along the ~ 0.5 arcmin length of the linear feature (see Fig. 3b) is shown in Fig. 7 (bottom right panel). The velocity gradient along the disjoint linear feature G0.162 + 0.159 shows an increase to the north and is ~ 1 km s^{-1} per arcsec or ~ 25 km s^{-1} pc^{-1}.

Numerous molecular surveys of the Galactic Centre show high-velocity gas in the general direction of G0.17+0.15 (Bally et al. 1988; Sofue 1995; Oka et al. 1998; Henshaw et al. 2016; Sormani et al. 2019; Veena et al. 2023). Due to the mismatch with our high-resolution data, it is difficult to associate large-scale molecular gas with the H II region. We found no evidence of far-IR emission at
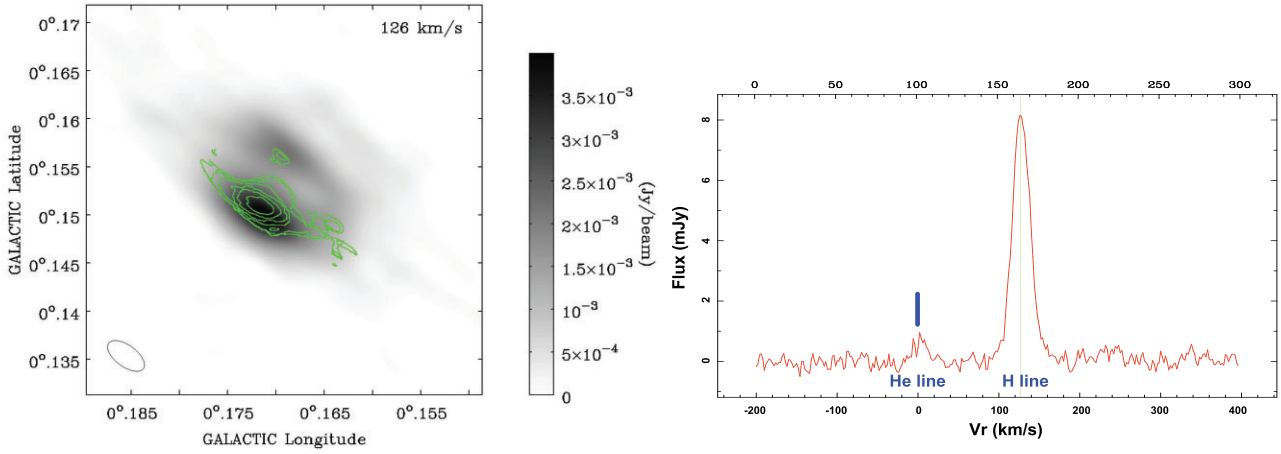
Figure 5. *(Left a)* The channel image with the peak intensity of RRL at 126 km s^{-1}. The contours (green) represent the intensity of helium RRL flux 0.5 mJy beam^{-1} km s^{-1} × (3, 4, 6, 8, 10, and 12). An open ellipse is shown at the bottom-left corner corresponding to the synthesized beam 16 arcsec × 8 arcsec (PA = 53.5°). *(Right b)* The line profile towards the region with the line peak. The hydrogen line peak is located at 126 km s^{-1}, marked with a green vertical line). The corresponding helium line is detected at near 0 km s^{-1} for the hydrogen line but not for the helium line, marked with a blue bar. With a 4σ cutoff, we integrated the helium line flux from the channels at velocities between -18 and $+18$ km s^{-1}, as shown in the contour image. The top axis is labelled with the channel serial numbers of the spectral cube.

≥ 100 µm that would be indicative of cold ($T \lesssim 20$ K) dust from the direction of G0.17+0.15 using Herschel data. At 120–140 km s^{-1}, the nearest bright CO clumps are about $\sim 0.1°$ away. However, there is diffuse molecular gas in the direction of G0.17+0.15 at velocities between 120 and 140 km s^{-1} (Oka et al. 1998). In spite of a lack of cold dust emission at the far-IR, the comparison of the CO molecular complex and the H II region suggests that G0.17−0.15 could be a star-forming site embedded within the CO cloud. Future higher spatial resolution molecular line observations would be capable of revealing a the possible association of the CO cloud complex with G0.17+0.15.

To summarize, a number of kinematic arguments support the interaction picture. One is the evidence for the highest velocity ionized gas with a velocity gradient along the direction of the linear feature, as noted to the north-west of the ring. This feature is disjoint from the H II region, likely to be ablated from the southern shell of G0.17+0.15, and accelerated in the direction of the filaments. Second, the evidence for stronger continuum and recombination line intensities, higher radial velocity and higher velocity dispersions in the southern shell of the ring when compared to the northern shell, all suggest the possibility that the gas in the southern shell is kinematically disturbed as a result of the interaction with NRFs. The above morphological and kinematic arguments are plausible; however, we have no direct proof of the interaction picture.

3.1.4 Electron temperature

Using equation (1) of Zhao, Blundell & Moran et al. (2010), from the RRL (I_{RRL}) and continuum ($I_{H II}$) images, a distribution of the electron temperature (T_e^*) was computed (Fig. 8a), assuming the ionized gas is under local thermodynamic equilibrium (LTE) conditions (e.g. Wilson, Rohlfs & Hüttemeister 2009). Based on the rms noises of RRL and continuum images, an error in T_e^* was also computed (Fig. 8b). The typical values of T_e^* are in the range between 7 and 10×10^3 K, with a 10–20 per cent uncertainty within the H II region. The contamination from the synchrotron radiation (I_{syn}) leads an uncertainty in the T_e^* calculation. Within the H II region with higher thermal electron density, the error due to the extended synchrotron emission is at a

level of 10 per cent, which is not included in image of T_e^*-error. In the diffuse area surrounding the H II region, for example around the shell of the H II region and the south-west (G0.162 + 0.156), the ratio of $I_{syn}/I_{H II}$ drastically increases. The derived high values of T_e^* in these regions are upper limits because significant contribution from synchrotron emission in the measured continuum flux density. Thus, an accurate measure of the electron temperature in the region where highest velocity is noted is not possible.

3.1.5 In-band spectral index (α) at 1.28 GHz

Figs 9(a) and (b) show spectral index (α) images, where the flux density is $S_\nu \propto \nu^\alpha$, using unfiltered and filtered MeerKAT channel maps, respectively. The low-resolution (8 arcsec) spectral index image in Fig. 9(a) shows that the ring has a flat spectrum, $\alpha \approx -0.1$, consistent with being a thermal source (Heywood et al. 2022). Diffuse emission to the north of G0.17+0.15 also shows the spectrum of thermal emission. The spectral indices of the non-thermal filaments surrounding the H II region are fairly flat as well. Fig. 9(b) shows spectral indices derived from filtered images. With backgrounds subtracted, no spectral indices can be calculated for broad diffuse regions. The median spectral indices for the detected non-thermal filaments are overplotted. The filaments at the western edge of the ring have steeper spectral indices, $-0.5 < \alpha < -0.3$ than the isolated, short westernmost filament G0.146 + 0.14 with $\alpha \approx -0.18$. Altogether, the filaments of the Radio Arc and its extension have flatter median spectral index values than those found in the Galactic Centre radio bubble, which have mean spectral index $\alpha \approx -0.83$ (Yusef-Zadeh et al. 2022).

3.1.6 In-band spectral index at 10 GHz

Using the 11 sub-band images of *X* band, we computed a set of α_{ij} images. An in-band average of α_{ij} is computed with the WASC algorithm. Fig. 10 shows a result from WASC for the distribution of spectral index. The relatively lower resolution image, good for sampling the diffuse emission, shows a significant gradient in α across the H II region. A $5\sigma_\alpha$ filter has been applied to the α images.
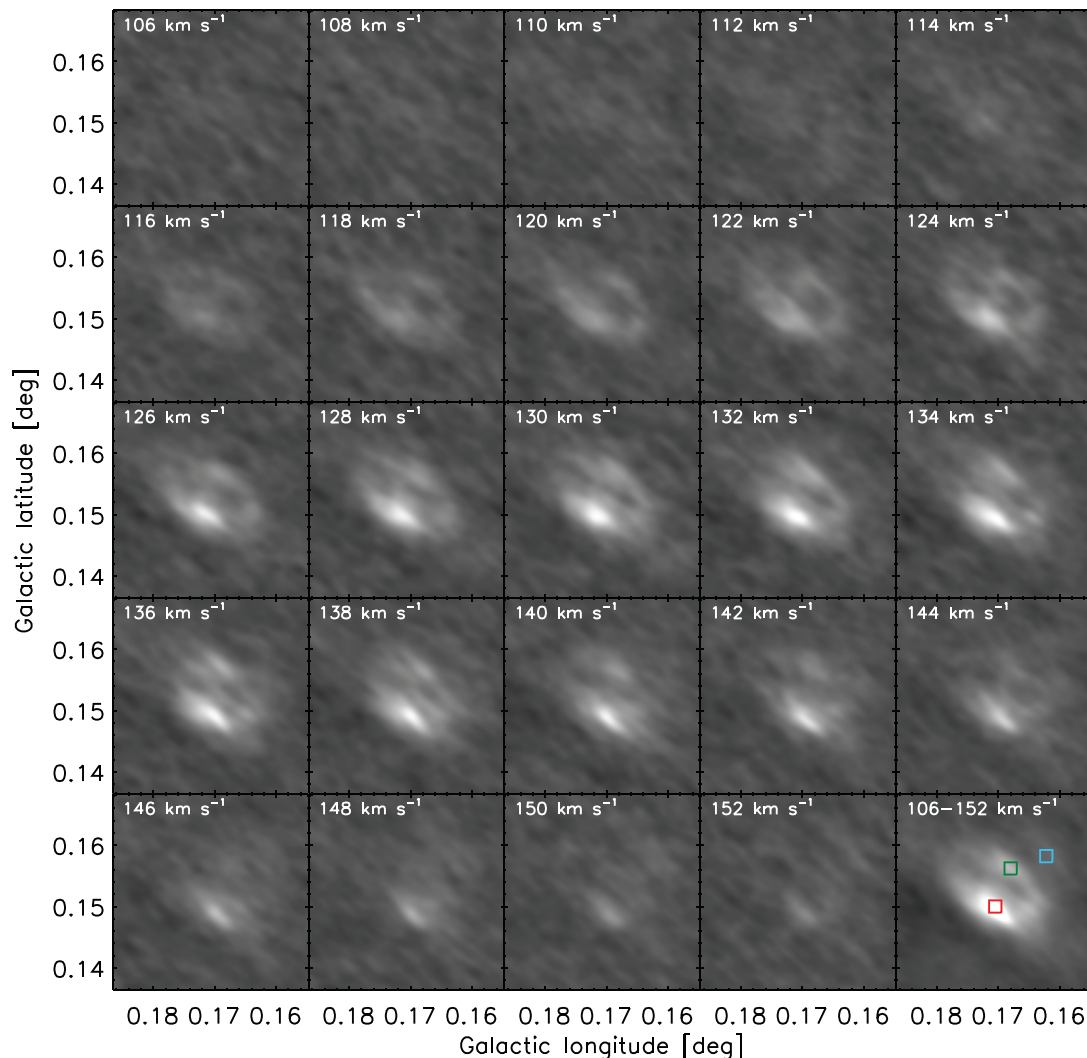
Figure 6. VLA image of the stacked RRL (H92α −H82α) from the H II region in G0.17+0.15 at 10 GHz, $\sigma_{\rm rms} = 65\ \mu$Jy beam^{-1} ch^{-1}. The image is convolved with a beam of FWHM = 16 arcsec × 8 arcsec (53.6° in Galactic coordinates). The LSR velocities are indicated in each panel. The velocity increment is $\Delta V = 2$ km s^{-1} from left to right. The integrated line intensity is shown in bottom right corner. The squares show the locations of three spectra displayed in Fig. 7.

The steeper spectrum of the emission to the west of G0.17+0.15 could be the result of the contamination by diffuse non-thermal emission.

3.1.7 Rotation measure (RM)

Single dish observations of the entire eastern edge of the radio bubble with an extent of 2° have determined the RM distribution, inferring that the intrinsic direction of the magnetic field traces vertical filaments perpendicular to the Galactic plane (Inoue et al. 1984; Seiradakis et al. 1985; Tsuboi et al. 1986). The RM is an integrated product of the electron density and the magnetic field component along the line of sight. RM values are negative over the entire two degrees of the Radio Arc and its northern and southern extensions with the exception of the region surrounding G0.17+0.15, where the RM is positive. The RM changes from a range of values between −500 and −1000 rad m^{-2} to 500 and 1000 rad m^{-2} at the western edge of G0.17+0.15 and its northern extension (Tsuboi et al. 1986). This change coincides with the region where the spectral index values show both thermal and non-thermal emission. It is possible

that entrainment of the G0.17+0.15 cloud injects thermal electrons in the positive latitudes of the GCL, changing the spectral index and stretching the magnetic field lines, thus making the sign of the RM change. The magnetic field direction could change from being slightly tilted away from the line of sight to being slightly tilted towards the line of sight. For a typical 100 μG magnetic field strength, and a 2-pc path length, this would only require electron density $n_{\rm e}$ > 10 cm^{-3}. The RM change and the magnetic field bending near G0.17+0.15 provide additional support for the interaction of non-thermal filaments with G0.17+0.15.

3.1.8 IR and spectral tomography images

Fig. 11(a) shows an RGB colour image of G0.17+0.15 at 20 cm, 8 μm, and 5.6 μm. The *Spitzer* IRAC images show diffuse IR emission extending over the entire radio structure, with a rising spectrum between 5.8 and 8 μm, so red in IR colour.

To see whether there was a radio counterpart to the IR structure, we applied the spectral tomography technique of Katz-Stone & Rudnick (1997) to the MeerKAT data. In this technique, a series of residual
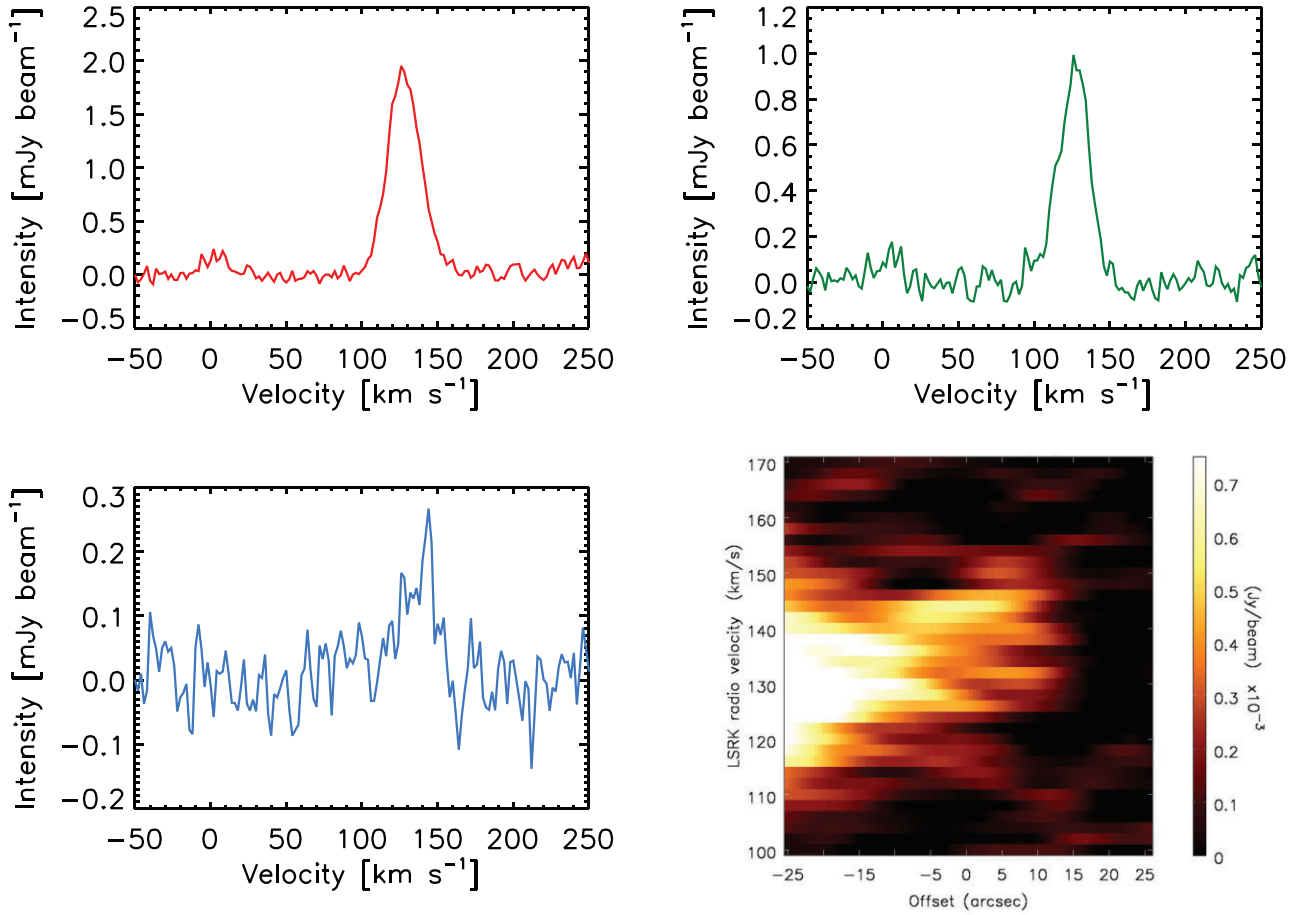
Figure 7. The spectra of RRL emission from G0.17+0.15 are presented towards three positions, as shown by squares in blue, red, and green squares (see text). The bottom right panel shows the position velocity (PV) diagram along the linear feature to the west of G0.17+0.15. The area from which the PV is generated is shown by two parallel lines (see Fig. 2a) with roughly a 0.17 and 0.5 arcmin width and length, respectively, with PA = 180°. The positive offsets are at higher latitudes than negative offsets. The diagram covers the velocity range between 100 and 170 km s^{-1}.
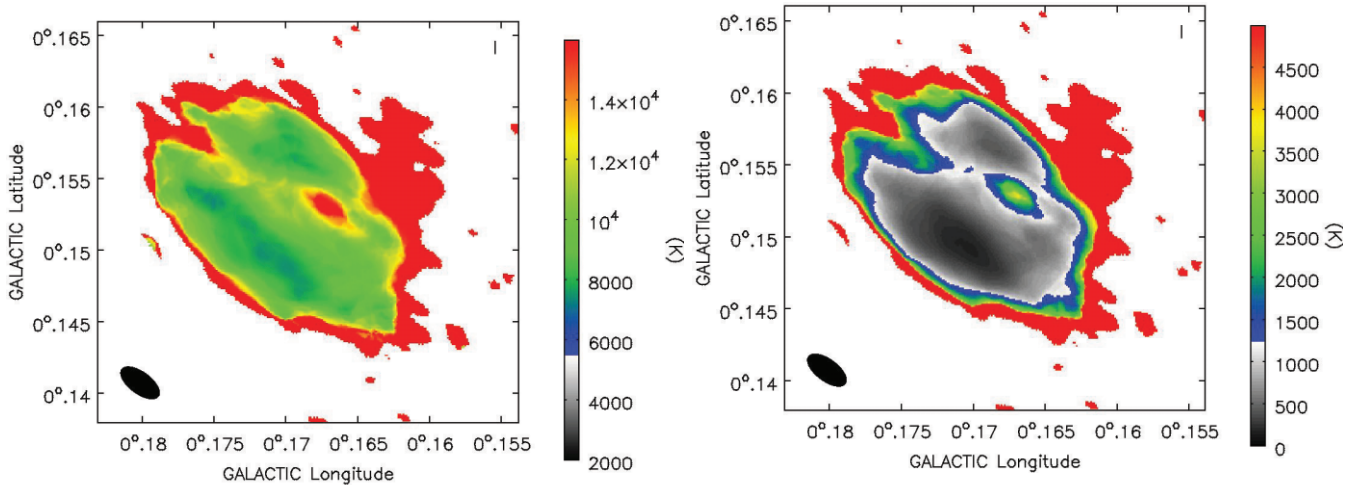

Figure 8. *(Left a)* The T_e* derived from RRL and continuum data observed with the VLA in C and D array configuration at 10 GHz, assuming the electrons are under the LTE condition and the density ratio of helium to hydrogen is 0.07. *(Right b)* σ_{T_e*}, the errors of the T_e* image derived from 1σ rms noises of the RRL and continuum images. The synthesized beam is marked as a filled ellipse in the bottom left of the plots.
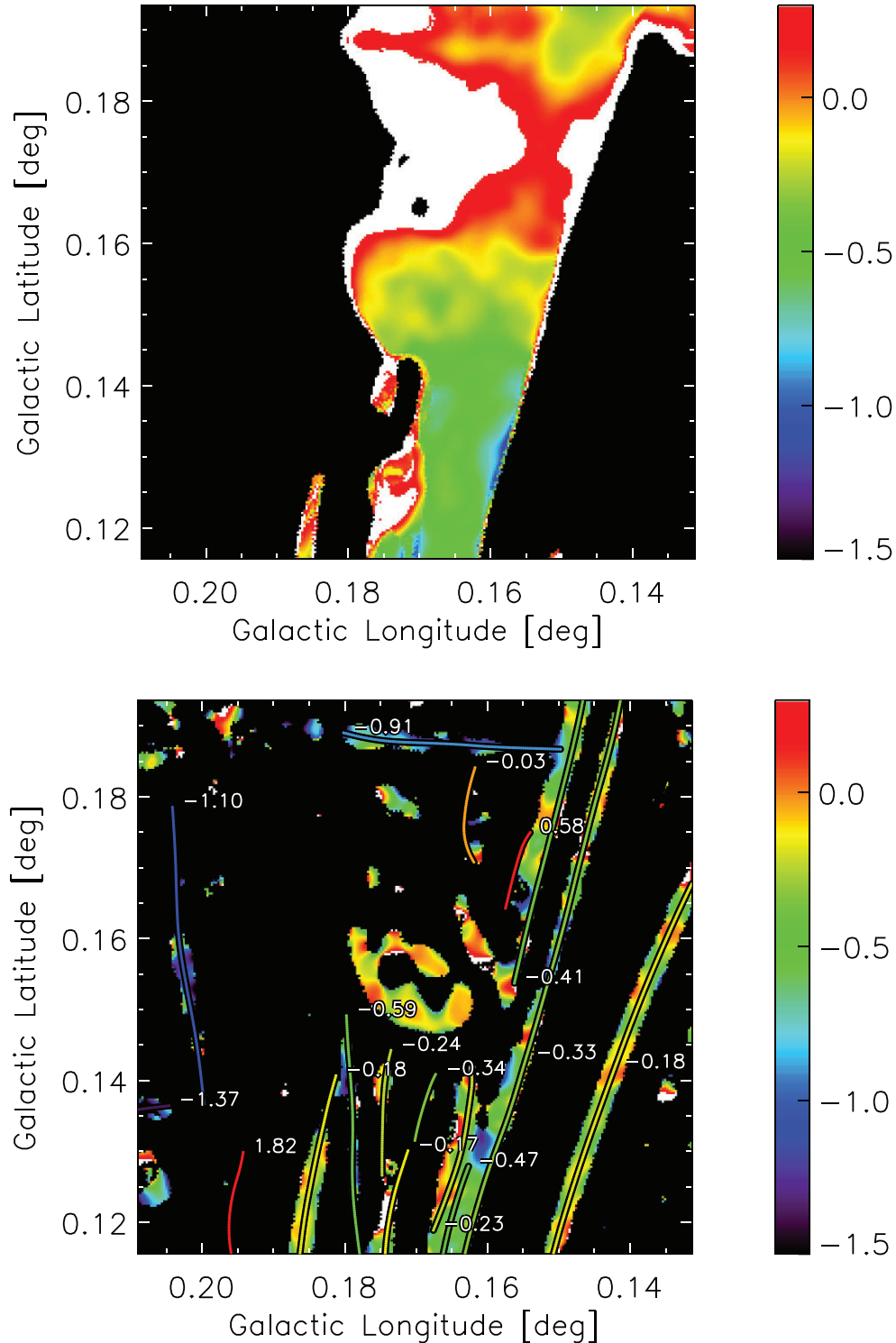
Figure 9. *(Top a)* Spectral indices of G0.17+0.15 and NRFs using non-filtered data cubes centred at 1.28 GHz. White regions show $\alpha > 0.3$, whereas black regions had no sufficient data and were masked. *(Bottom b)* Similar to (a) except filtered data cubes were used. The spectral index image using filtered data cubes is overlaid with the median spectral index traced along each detected filament. The scale bar to the right shows the spectral index values from -1.5 to $+0.3$.

images is created by removing all of the emission with a specific spectral index (α_t).[1] In the residual images for $\alpha_t = 0 \pm 0.05$, the

ring is no longer visible, so the spectrum of the ring is essentially flat. The residual emission is shown in Fig. 11(b). It peaks up inside

---

[1]To construct the residual images, we subtracted an image of the average of 8 arcsec MeerKAT channels 11, 12, and 14 (effective frequency 1542.4 MHz)

from the average of channels 0–3 (962.85 MHz), with scale factors corresponding to a range of spectral indices, $-1.5 < \alpha_t < 0.35$.
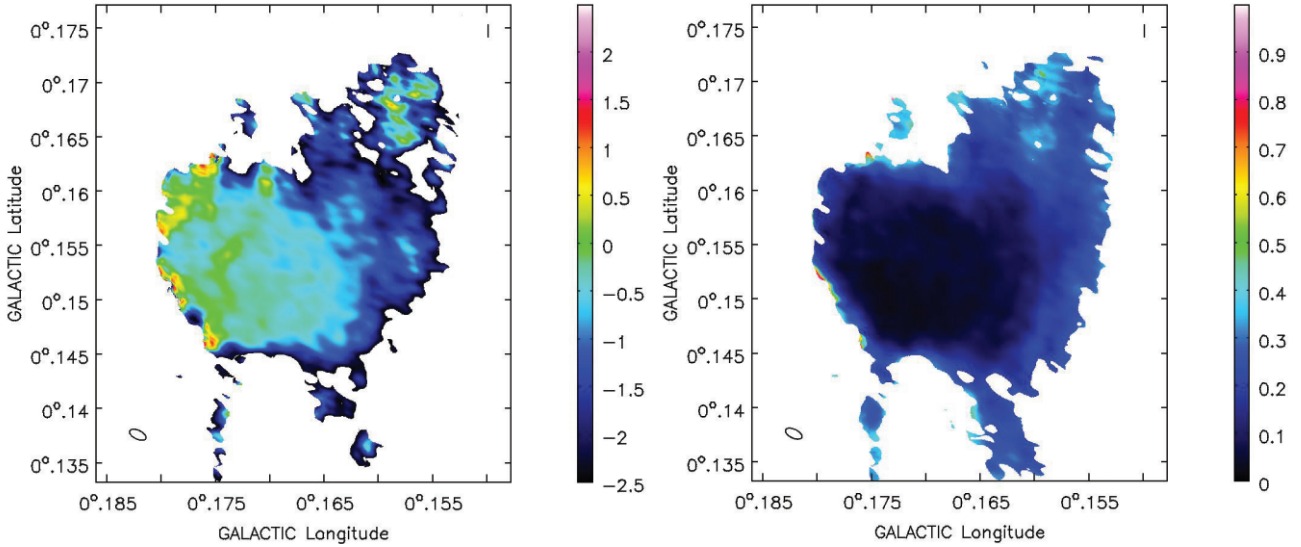
Figure 10. *(Left a)* An image of in-band spectral index α computed from the VLA *X*-band data observed in the C- and D-array configurations. *(Right b)* The corresponding one σ error σ_α. The beam size is FWHM = 5.9 arcsec $\times$ 2.9 arcsec (6°). A $5\sigma_\alpha$ cut-off is applied for both images. The display ranges are [−2.5, 2.5] for the spectral index α and [0, 1] for the 1σ uncertainty of the spectral index. The synthesized beam is marked as an open ellipse in the bottom left of the plots.

of the ring, and is therefore somewhat steeper, and has a location and extent similar to the diffuse IR feature in Fig. 11(a). This diffuse radio component has a spectral index of $\sim$−0.2, as determined from when it disappears from the tomography images.

The spectral indices of the ring and its interior are different, suggesting different origin. The interior emission could be produced either by shocked stellar winds from a stellar source embedded within the ring or by large-scale cosmic ray-driven nuclear wind interacting with an H II region and diffusing into the H II region.

3.1.9 SEDs of nearby sources

The diffuse IR source that comprises the entirety of G0.17+0.15 is saturated in the *Spitzer* MIPS 24 μm image, but has unsaturated mid-IR measurements from IRAS, MSX, *WISE*, and *Herschel* (see Fig. 11a). To determine the energetics of this source, the IRAS 25 and 60 μm data points of the Spectral Energy Distribution (SED) were fit as either silicate or amorphous carbon dust grains at a single temperature. These fits, shown in Fig. 11(a), provide estimated dust temperatures of $T = 56$ or 66 K, for silicate or carbon, respectively. The implied dust masses are 0.10 M$_\odot$ for silicate or 0.067 M$_\odot$ for amorphous carbon. Assuming a dust/gas mass ratio of 0.0062, the implied gas masses are 16 and 11 M$_\odot$. Dust and gas masses may be higher if a cooler component is present, but the lack of detection at 100 and 160 μm suggests that there is not a significant colder component. The mid-IR luminosity of this source is $\sim$2 $\times$ 10^4 L$_\odot$.

Using higher resolution 2MASS and *Spitzer* IRAC data, we explored the SEDs of IR sources in the 2 arcmin vicinity of the H II region. In addition to ubiquitous stars, mid-IR images also reveal emission associated with G0.17+0.15, as seen in the composite radio and IR image in Fig. 11(a). There are two unusual IR sources in the centre of G0.17+0.15. The first is slightly more extended than a point source and appears coincident with a compact radio peak. This source has very red IR colours and is only catalogued at 5.8 and 8 μm. It is the yellow-green blob, indicated by green tick marks on Fig. 11(a). Its SED is shown by the heavy black circles and line in

Fig. 12(a) (left panel). The second unusual source appears point-like, and is displaced about 2 arcsec to the west. It is a relatively faint bluish source, partially merged with the preceding source, in Fig. 11(a). It is only detected at 1.25–5.8 μm. Coincidentally, its 5.8 μm flux density is very similar to that of the preceding source. Its SED is shown by circles and black line lines in Fig. 12(b) (right panel), and shows an unusual excess in emission at 3.6–5.8 μm compared to all of the other stellar sources in the 2 arcmin vicinity. These are the (a) and (b) choices discussed in the next paragraph.

The presence of a distinctive central source (perhaps two) suggests that the ring of G0.17+0.15 might not be an H II region associated with star formation, but rather the result of mass-loss from an evolving high-mass star. Shells with a somewhat similar appearance and SEDs are seen around the LBV stars such as the Pistol star and LBV 3 in the Galactic Centre and RMC 143 in the Large Magellanic Cloud (Lau et al. 2014; Agliozzo et al. 2019). There are two choices for the responsible source: (i) It may be coincident with the radio source having a diffuse, red, IR counterpart. The IR would suggest the source is deeply embedded in a cloud, making it perhaps unlikely that the star's UV radiation could escape to ionize the ring. In this scenario, the Arches cluster may ionize the H II region externally. This is analogous to the Pistol nebula being photoionized externally by the Quintuplet cluster star (Lau et al. 2014, and references therein). The implied mass of 11–16 M$_\odot$ lost by the star is somewhat high, but the estimate could be reduced if the dust-to-gas mass ratio in the circumstellar material is higher than typical for the interstellar medium. (b) The near-IR point source may be the source of ionization. There is far less circumstellar material here. UV radiation could escape to ionize the ring and may also provide an external heating source for dust in the nearby diffuse IR source.

In either case, an additional constraint can be placed by estimating the number of Lyman continuum photons needed for a stellar source to ionize the gas. Assuming an electron temperature of 8000 K, and a distance of $\sim$8 kpc from us and a flux density of $\sim$0.3 Jy, the total estimated Lyman continuum rate is 1.6 $\times$ 10^{48} photons s^{-1}. Assuming that the emission is produced by a single zero-age
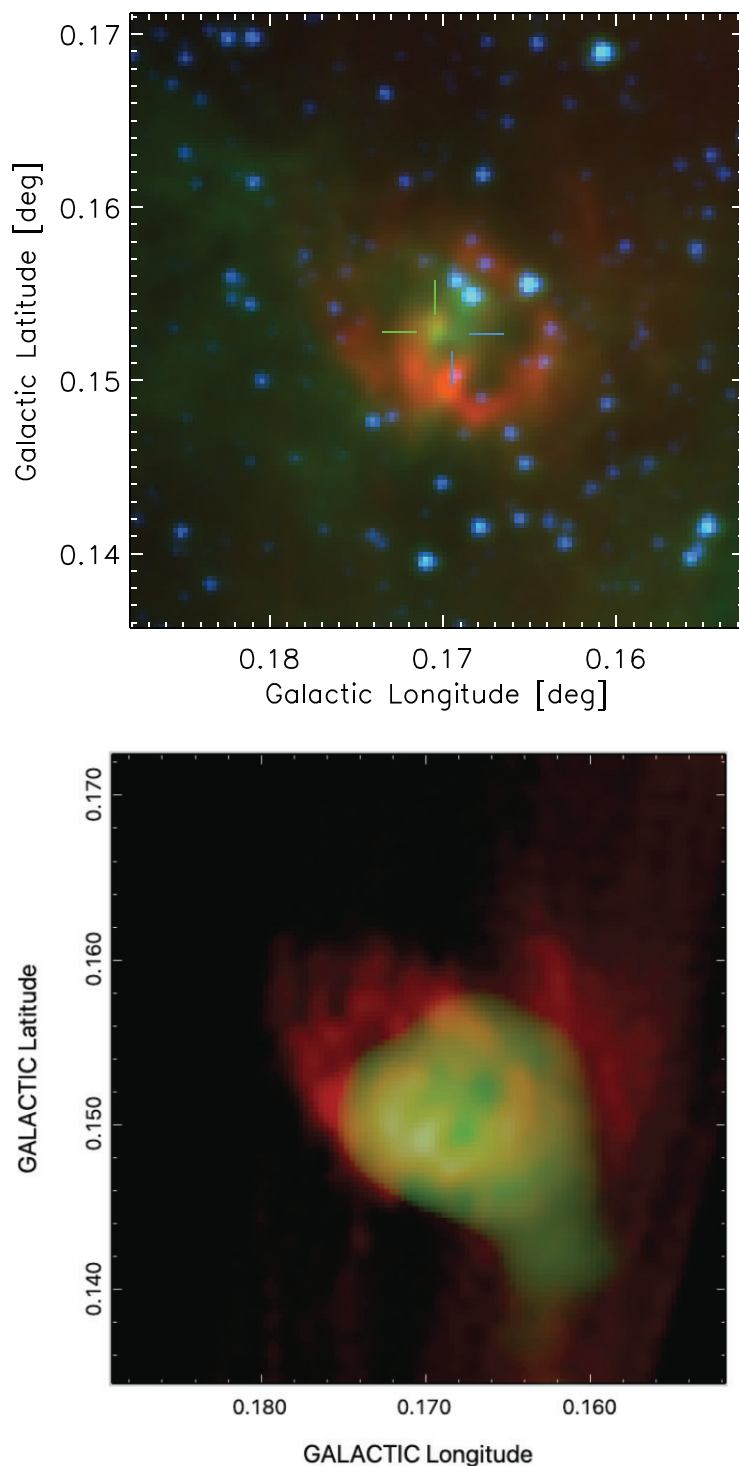
Figure 11. *(Top a)* A composite RGB colour image of G0.17+0.15 is shown at 20 cm (R), 8 μm (G), and 5.8 μm (B). The radio source close to the centre of the H II region has a diffuse 8 μm counterpart. Green and blue tick marks indicate the locations of the two possible central IR sources that are discussed in the text. *(Bottom b)* MeerKAT radio images of total intensity (red, as in Fig. 11a) at 4 arcsec resolution, overlaid with the residual radio emission in green, at 8 arcsec resolution, after removing all of the radio emission with $\alpha = 0$, as described in the text.

main-sequence (ZAMS) star, a spectral type of O8-9 would produce sufficient ionizing photons to drive the emission (Panagia 1973). If the star is an evolved supergiant, then a later spectral type of B0 can produce the same ionizing flux. The total stellar luminosity is $\sim 5 \times 10^4 \, \mathrm{L}_\odot$, for a ZAMS star (or up to $\sim 3 \times 10^5$ for a supergiant), sufficient to produce the dust luminosity estimated above.

4 DISCUSSION

An implication of the physical association of high-velocity, diffuse H II gas and molecular clouds with the eastern and western lobes, respectively, is that the lobes, the radio bubble, and NRFs are located at the Galactic Centre. Two features that need to be addressed
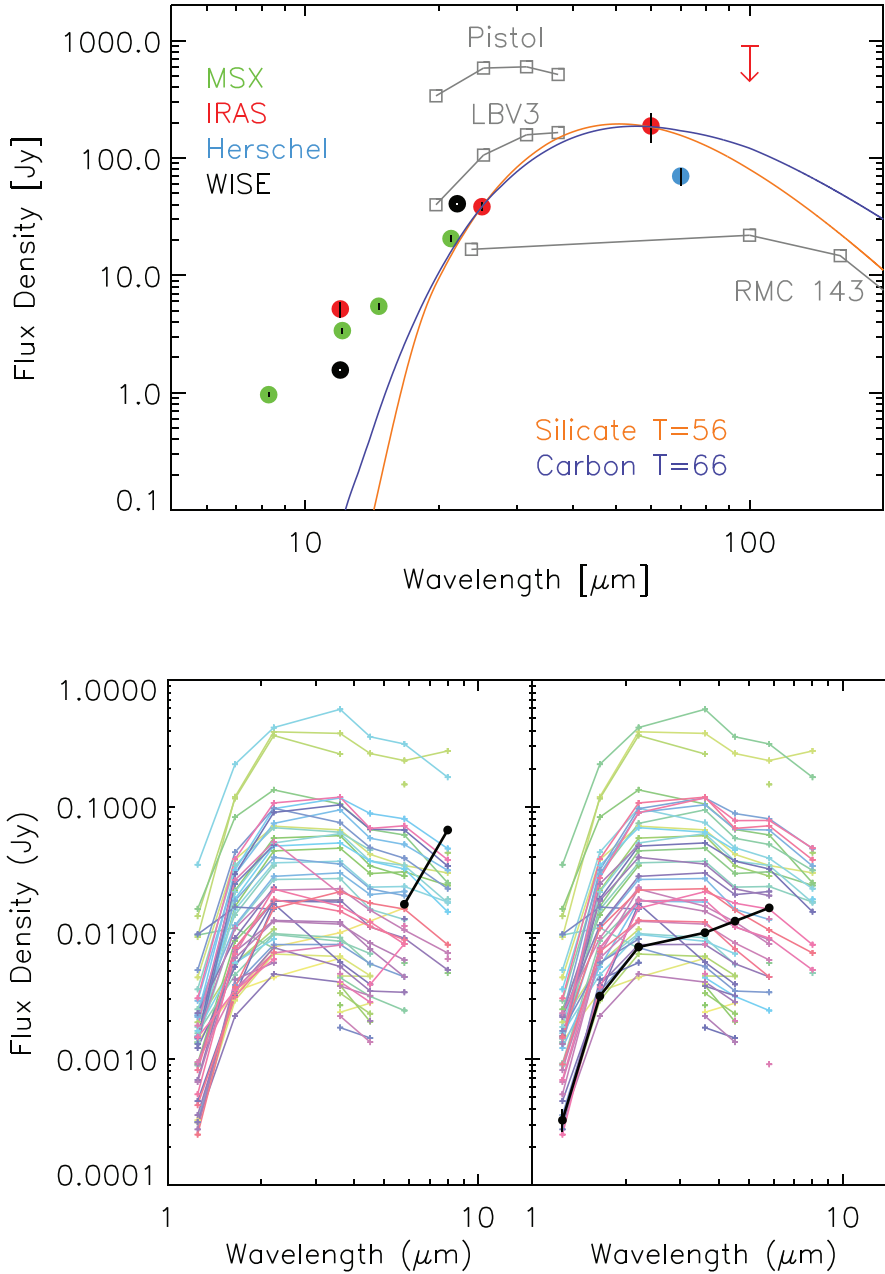
Figure 12. *(Top a)* The SED of G0.17+0.15 as taken from various catalogues where the source is essentially unresolved (point-like sources). In the *WISE* catalogue, the source is resolved into multiple components, but the one plotted is dominant at 12 and 22 μm. A single-temperature fit to the IRAS 25 and 60 μm data points is shown for either silicate or amorphous carbon dust grains. Grey SEDs for comparison are those of the shells around 3 LBV stars (Lau et al. 2014; Agliozzo et al. 2019). Error bars are added to the G0.17 measurements. The error bars are generally smaller than the plotted symbols (solid circles). *(Bottom b)* The heavy black SED in the left panel is that of the diffuse central source (indicated by green tick marks in Fig. 11a) as listed in 2MASS and *Spitzer*/IRAC catalogs. The other SEDs plotted are the field stars within a 2 arcmin radius (randomly coloured for clarity), showing that no other nearby sources have a similar SED. The black line in the right panel shows that the SED of the bluer central point-like source (indicated by blue ticks in Fig. 11a) has a strong excess at >3.6 μm that is not present in any of the field stars.

are whether the H II region G0.17+0.15 is interacting with NRFs, as well as being accelerated by the ram pressure of cosmic ray driven outflow directed along the non-thermal filaments. The radio bubble hosts hundreds of mysterious magnetized radio filaments, the largest concentration of which is the radio arc. The decline in the number of filaments as a function of Galactic longitude and latitude are consistent with the size of the radio bubble, suggesting a causal association with the origin of the filaments (Heywood et al.

2019). One scenario for the origin of the bipolar radio/X-ray features involves a high cosmic ray pressure driving large-scale winds and expanding the medium away from the Galactic plane (Yusef-Zadeh & Wardle 2019). The cosmic ray ionization rate in the Galactic Centre is two to three orders of magnitudes higher than in the Galactic disc, implying that the cosmic ray pressure is sufficient to launch a nuclear wind from the Galactic Centre (Yusef-Zadeh & Wardle 2019).

The above interpretation is not unique. It is possible that infall motion of the cloud and/or H II region from its high-latitude location towards the Galactic Centre, can explain some of the observed features. In this picture, G0.17+0.15 is formed in the clumpy large-scale molecular cloud. However, if G0.17+0.15 were part of a larger cloud that is falling into the disc of the Milky Way, then it is an unfortunate coincidence that it is superimposed on the radio arc at relatively low latitudes of ~0.15°, and that there are no other similar structures elsewhere in the CMZ.

Here, we only focus on plausibility of the nuclear wind. We assume that the interacting nuclear wind can explain the cause of morphological and kinematical asymmetry in G0.17+0.15.

4.1 Asymmetric ablation of the western edge of the ring

We made a number of morphological and kinematic arguments of an asymmetry in the radial velocity field and brightness distribution across the width of G0.17+0.15. The asymmetry suggest that the ionized gas could be ablated by an external ram pressure of the nuclear wind as traced by a larger concentration of the filaments at the western edge of the H II region. The electron density n_e from the western side of the ring is estimated to be $\sim 300\,\text{cm}^{-3}$ using an intensity of ~7 mJy per 4 arcsec beam at 1.28 GHz. The mass of ionized gas in G0.17+0.15 is then ~20 $M_\odot$, consistent with the dust mass inferred above.

Using a velocity difference of $\delta v \sim 15\,\text{km s}^{-1}$ across the diameter of the ring, $L \sim 1.5$ pc, and the ionized gas density of $n_e \sim 3 \times 10^2$ cm^{-3}, the needed ram pressure, is $500\,\text{eV cm}^{-3}$, which is comparable to the $\sim 10^3\,\text{eV cm}^{-3}$ cosmic ray driven wind pressure needed to explain X-ray filled radio bubble (Yusef-Zadeh & Wardle 2019) and consistent with a scenario in which this wind is responsible for the ablation. The thermal pressure of the ionized gas for $n_e = 300$ cm^{-3} and 8000 K is $450\,\text{eV cm}^{-3}$, so the H II region is likely to be confined by its surroundings.

In the above picture, the gas streamers on the western side of the H II region are stripped and assumed to have been uniformly accelerated from 0 to $\delta v \sim 35\,\text{km s}^{-1}$ over a length of $l \sim 1.4$ pc. The acceleration is $0.5 \times \delta v^2 / l$ over a time-scale $2 \times l/\delta v$, which is roughly 8×10^4 yr. The estimated column density of the ablated material $\sim 5 \times 10^{20}$ cm^{-2}, implies that the required ablating ram pressure is $\sim 700\,\text{eV cm}^{-3}$, which is also comparable to the $\sim 10^3\,\text{eV cm}^{-3}$ cosmic ray driven wind pressure.

5 SUMMARY

We studied G0.17+0.15, lying in the eastern (positive Galactic longitudes and high Galactic latitudes) lobe of the Galactic Centre, respectively. Although there are other ideas that can explain its structure, the kinematics and origin, our focus was mainly on the H II region G0.17+0.15, because of its high radial velocity $\sim 130\,\text{km s}^{-1}$. Based on its morphology, kinematic, and polarization measurements, we provided arguments for the interaction of G0.17+0.15 with a number of NRFs which themselves are considered to be accelerated by a cosmic ray driven wind inflating the Galactic Centre radio bubble. As such, the properties of G0.17+0.15 are consistent with entrainment. Velocity gradients along the linear features to the west of G0.17+0.15, as being ablated by the cosmic ray driven nuclear wind. We also found two IR sources within G0.17+0.15. The presence of a distinctive central source may be an indication of mass-loss from an evolving high-mass star. The SED of this red source appears to be similar to that of LBV stars such as the Pistol star and LBV 3 in the Galactic Centre.

The above ideas are not unique in explaining G0.17+0.15. It is possible that G0.17+0.15 is a site of star formation in high-velocity orbiting molecular clouds and that massive stars are formed in the clumpy molecular environment of the Galactic Centre. Future high-resolution radio and IR observations will be able to test the physical association of G0.17+0.15 and large-scale molecular clouds and identify whether massive or evolved stars power the H II region.

DATA AVAILABILITY

All the data including MeerKAT that we used here are available online and are not proprietary. We have reduced and calibrated these data and these are available if requested.

REFERENCES

Agliozzo C. et al., 2019, A&A, 626, A126
Alves M. I. R., Calabretta M., Davies R. D., Dickinson C., Staveley-Smith L., Davis. R. J., Chen T., Barr A., 2015, MNRAS, 450, 2025
Bally J., Stark A. A., Wilson R. W., Henkel C., 1988, ApJ, 324, 223
Briggs D. S., 1995a, PhD Theory
Briggs D. S., 1995b, BAAS, 27, 1444
Conway J. E., Cornwell T. J., Wilkinson P. N., 1990, MNRAS, 246, 490
Crocker R. M., Aharonian F., 2011, Phys. Rev. Lett., 106, 101102
Di Teodoro E. M., McClure-Griffiths N. M., Lockman F. J., Armillotta L., 2020, Nature, 584, 364
Everett J. E., Schiller Q. G., Zweibel E. G., 2010, ApJ, 711, 13
Henshaw J. D. et al., 2016, MNRAS, 457, 2675
Heywood I. et al., 2019, Nature, 573, 235
Heywood I. et al., 2022, ApJ, 925, 165
Högbom J. A., 1974, A&AS, 15, 417
Inoue M., Takahashi T., Tabara H., Kato T., Tsuboi M., 1984, PASJ, 36, 633
Katz-Stone D. M., Rudnick L., 1997, ApJ, 488, 146
Kulsrud R. M., Cesarsky C. J., 1971, ApL, 8, 189
Lang C. C., Goss W. M., Morris M., 2001, AJ, 121, 2681
Lau R. M., Herter T. L., Morris M. R., Adams J. D., 2014, ApJ, 785, 120
Law C. J., Backer D., Yusef-Zadeh F., Maddalena R., 2009, ApJ, 695, 1070
Lockman F. J., Di Teodoro E. M., McClure-Griffiths N. M., 2020, ApJ, 888, 51
McClure-Griffiths N. M., Green J. A., Hill A. S., Lockman F. J., Dickey J. M., Gaensler B. M., Green A. J., 2013, ApJ, 770, L4
Oka T., Geballe T. R., 2020, ApJ, 902, 9
Oka T., Hasegawa T., Sato F., Tsuboi M., Miyazaki A., 1998, ApJS, 118, 455
Oka T., Geballe T. R., Goto M., Usuda T., McCall B. J., 2005, ApJ, 632, 882
Oka T., Geballe T. R., Goto M., Usuda T., Benjamin, McCall J., Indriolo N., 2019, ApJ, 883, 54
Panagia N., 1973, AJ, 78, 929
Pauls T., Mezger P. G., 1980, A&A, 85, 26
Ponti G. et al., 2019, Nature, 567, 347
Rau U., Conwell T. J., 2011, A&A, 532, A71
Royster M. J., Hewitt J. W., Roberts D. A., Yusef-Zadeh F., 2011, in Morris M. R., Wang Q. D., Yuan F., eds, ASP Conf. Ser Vol. 439, The Galactic Center: a Window to the Nuclear Environment of Disk Galaxies. Astron. Soc. Pac., San Francisco, p. 31
Seiradakis J. H., Lasenby A. N., Yusef-Zadeh F., Wielebinski R., Klein U., 1985, Nature, 317, 697

Sofue Y., 1995, PASJ, 47, 527
Sofue Y., Handa T., 1984, Nature, 310, 568
Sormani M. C. et al., 2019, MNRAS, 488, 4663
Su M., Slatyer T. R., Finkbeiner D. P., 2010, ApJ, 724, 1044
The CASA Team, 2022, PASP, 134, 114501
Tsuboi M., Inoue M., Handa T., Tabara H., Kato T., Sofue Y., Kaifu N., 1986, AJ, 92, 818
Tsuboi M., Tsutsumi T., Kitamura Y., Miyawaki R., Miyazaki A., Miyoshi M., 2020, PASJ, 72, L10
Veena V. S. et al., 2023, A&A, 674, L15
Veilleux S., Cecil G., Bland-Hawthorn J., 2005, ARA&A, 43, 769
Wilson T. L., Rohlfs K., Hüttemeister S., 2009, Tools of Radio Astronomy, 5th edn. Springer, Berlin, p. 369
Yang H.-Y. K., Ruszkowski M., Zweibel E., 2013, MNRAS, 436, 2734
Yusef-Zadeh F., 2012, ApJ, 759, L11
Yusef-Zadeh F., Morris M., 1988, ApJ, 329, 729
Yusef-Zadeh F., Wardle M., 2019, MNRAS, 490, L1
Yusef-Zadeh F., Morris M., van Gorkom J. H., 1987, AIP Conf. Proc. Vol. 155, Spatial and Kinematic Structure of the Thermal Components of the Galactic Center Arc. Am. Inst. Phys., New York, p. 190
Yusef-Zadeh F., Arendt R. G., Wardle M., Heywood I., Cotton W., Camilo F., 2022, ApJ, 925, L18
Zhao J.-H., Blundell R., Moran J. M., Downes D., Schuster K. F., Marrone D. P., 2010, ApJ, 723, 1097
Zhao J.-H., Morris M. R., Goss W. M., 2019, ApJ, 875, 134
Zweibel E. G., 2017, Phys. Plasmas, 24, 055402

APPENDIX A

A.1 Stacking multiple α-transition lines from an hydrogen-like atom

The image cubes of 11 RRLs were stacked in order to enhance the signal-to-noise ratio. We investigated a few algorithms in stacking the RRL images for optimizing the sensitivity. Here is a description of how to weight the individual RRL image cubes in the stacking process concerned in this paper:

$$\overline{\mathbf{I}_{RRL}} = \mathbf{wt} \cdot \mathbf{I}_{RRL},$$

where $\mathbf{I}_{RRL}$ is a 1D image matrix and its element is a RRL image cube at an α-transition corresponding to a principle quantum number (n) of an hydrogen-like atom:

$$\mathbf{I}_{RRL} = \begin{pmatrix} I_{RRL}[0] \\ I_{RRL}[1] \\ \vdots \\ I_{RRL}[m] \end{pmatrix},$$

and the weight matrix:

$$\mathbf{wt} = \left(wt[0], wt[1], \ldots, wt[m] \right).$$

In the case of the *X*-band VLA data, m = 10 and *i* is a serial number of the $\mathbf{I}_{RRL}$ elements, where $i = 0, 1,...,$ and 10, corresponds to $n = 92$, 91,... and 82; and wt[i] is a statistical weight used in the process of stacking the multiple RRLs. The final resultant RRL image cube $\overline{\mathbf{I}_{RRL}}$ is a dot-product of the weighting matrix $\mathbf{wt}$ and the RRL image matrix $\mathbf{I}_{RRL}$. Three different weighting methods were considered in this paper:

(1) equal weighting or

$$wt[i] = \left(\sum i \right)^{-1};$$

(2) weighted by the reciprocal value (σ_i^{-2}) of a variance determined from a RRL image cube,

$$wt[i] = \frac{1}{\sigma_i^2} \left(\sum \frac{1}{\sigma_i^2} \right)^{-1};$$

and

(3) weighted by a quadratic power of an S/N ratio,

$$wt[i] = \left(\frac{I_i^p}{\sigma_i} \right)^2 \left(\sum \left(\frac{I_i^p}{\sigma_i} \right)^2 \right)^{-1}.$$

In above equations, σ_i and I_i^p denote an rms noise and peak line intensity of the *i*th element in the RRL image cube matrix. We found that weighting with a quadratic power of an S/N ratio or $\left(\frac{I_i^p}{\sigma_i} \right)^2$ gives the best sensitivity among the three stacked image cubes. The final RRL image cube computed from method (3) is improved in sensitivity by $\sim$10 per cent and $\sim$5 per cent as compared to the one produced with an equal weighting function and a weighting with the reciprocal value of a variance, respectively. The sensitivity of the stacked RRL image cube is improved by a factor of 4 as compared to that of an individual RRL cube. Thus, we adopted the stacked RRL image cube produced by weighting with a quadratic power of an S/N ratio.

A.2 VLA in-band spectral index

Both the VLA's *X*-band and *C*-band data have a broad frequency coverage of 4 GHz in bandwidth (*BW*), providing a large ratio of $\left[\frac{BW}{v_0} \right] = 0.67$ and 0.4 at 6 and 10 GHz, respectively. Wideband imaging with the Taylor expansion technique (e.g. Rau & Cornwell 2011) has constructed a multifrequency synthesis (MFS) image of the continuum emission. This has been achieved from a radio source via Taylor expansion's first term or TT0, providing deep images with a high dynamic range. The second term Taylor expansion (TT1) deals with the slope of spectrum distributed across a wideband, from which one can derive images for distributions of spectral index. However, this technique is challenging because (1) cleaning sidelobes for TT1 requires high signal-to-noise ratio due to the TT1 beam being orthogonal to that of TT0 (Conway, Cornwell & Wilkinson 1990) and (2) the wideband coverage makes the linear expansion inappropriate for a source with a non-linear spectrum. A higher order expansion is needed to interpret the spectrum curvature. Thus, the reliability for extended sources was uncertain, often owing to an inadequate signal-to-noise ratio. On the other hand, the classical method uses two images I_1 and I_2 produced from data observed at v_1 and v_2 in a narrow band ($\Delta v < < v_1$ and $\Delta v \ll v_2$) following a formula:

$$\alpha = \frac{\text{Log}(I_1/I_2)}{\text{Log}(v_1/v_2)}.$$

The VLA was designed via array configurations and receiver bands to provide options for users to observe a source in multiple observing runs resulting in an equivalent uv-sampling at two separate band frequencies. In principle, the narrow-band approach reduces the uncertainties in determination of spectral index for strong sources. Given a wideband observation, numerous sub-bands produced in a single observing run, from which one can produce a large number of spectral index α images from a combination of a frequency pair (v_i, v_j), where i or j is a serial number of sub-bands, an integer from 0, 1, 2,... to n, with a total number of $n + 1$ sub-bands. A total number of sub-bands is $n + 1$. For the VLA data taken at X- and C-bands, the corresponding $n + 1$ is 12 and 32. An assemble

of spectral index α_{ij} images can be computed using above formula as well as their errors σ_{ij}^{α} based one the rms noises of images and a separation of a frequency pair (ν_i, ν_j). We note that both α_{ij} and σ_{ij}^{α} are two-dimensional images with RA and Dec in the x and y axes. For example, for the complex H II region G0.17+0.15 at X band, $\alpha_{ij}(x, y)$ was derived from a pair of 5000 spectral images $I_i(x, y)$ and $I_j(x, y)$. Instead of fitting to the higher order terms in Taylor expansion, the spectral index α using the classical method involves only the first term (TT0) of the Taylor expansion products. In addition, the bandwidth of a sub-bands $\Delta\nu_i$ appears to be small enough, so a linear approaching is valid for the slope of a radiation spectrum. For example, $\Delta\nu_i$ is 64 and 128 MHz ($\Delta\nu/\nu = 0.006$ and 0.02) for the VLA X-band and C-band data. We also note that the sub-band data taken in a wideband observation are subject to the frequency-dependent issues in aperture synthesis interferometer imaging, such as primary beam attenuation, short-baseline cut-off and frequency smearing as well as radio frequency interference. Those effects are accounted for in the process of constructing α as well as by computing a weighted-average of a sub-band combination (WASC) of frequency-pair images α_{ij}. The statistical errors reflect the uncertainty of the algorithm.

This paper has been typeset from a TEX/LATEX file prepared by the author.